On the interfacial lithium dynamics in $Li_7La_3Zr_2O_{12}$:poly(ethylene oxide)(LiTFSI) composite polymer-ceramic solid electrolytes under strong polymer phase confinement

Mauricio Rincon Bonilla[a,*], Fabián A. García-Daza[b], Henry A. Cortés[a], Javier Carrasco[c], Elena Akhmatskaya[a,d]

[a]*BCAM - Basque Center for Applied Mathematics, Alameda de Mazarredo 14, E-48009 Bilbao, Spain*
[b]*Department of Chemical Engineering, The University of Manchester, Manchester M13 9PL, United Kingdom*
[c]*Centre for Cooperative Research on Alternative Energies (CIC energiGUNE), Basque Research and Technology Alliance (BRTA), Alava Technology Park, Albert Einstein 48, 01510, Vitoria-Gasteiz, Spain*
[d]*IKERBASQUE, Basque Foundation for Science, Plaza Euskadi 5, 48009 Bilbao, Spain*

Abstract

A better molecular-level understanding of Li^+ diffusion through ceramic/polymer interfaces is key to design high-performance composite solid-state electrolytes for all-solid-state batteries. By considering as a case study a composite electrolyte constituted by Li^+ conductive Ga^{3+} doped-$Li_7La_3Zr_2O_{12}$ (LLZO) garnet fillers embedded within a poly(ethylene oxide) and lithium bis(trifluoromethanesulfonyl) imide polymer matrix (PEO(LiTFSI)), we investigate Li^+ interfacial dynamics at conditions of high polymer confinement, with large filler particles in a fully amorphous polymer phase. Such confinement scenario is aimed to capture the conditions near the percolation threshold, at which conductivity enhancement is often reported. Using molecular dynamics simulations combined with the generalized shadow hybrid Monte Carlo method and umbrella sampling calculations, we explain why the hopping towards the polymer phase of the Li^+ sitting on the LLZO surface is thermodynamically hindered, while hopping of Li^+ from the polymer to the LLZO is kinetically slowed-down by rigidified polymer near the

---
[*]Corresponding author
Email address: `mrincon@bcamath.org` (Mauricio Rincon Bonilla)

interface. In addition, we demonstrate how the overlap of LLZO-bound polymer chains at high confinement leads to a decrease of Li^+ diffusivity within the interstitial space. We put forward that these insights are relevant to interpret the variation of ionic conductivity as a function of volume fraction and filler particle sizes also below the glass transition temperature of the polymer, at the typical operating conditions of lithium ion batteries.

Keywords: Polymer-Ceramic Electrolytes, Interfacial Lithium Transport, Solid-State Lithium ion Batteries, Hybrid Monte Carlo, Umbrella Sampling, Molecular Dynamics.

1. Introduction

All-solid-state Li-ion batteries, with a thin solid electrolyte might transform the energy-storage landscape, enabling the implementation of high capacity metal Li anodes and avoiding the use of flammable organic liquid electrolytes [1, 2]. Realizing this paradigm shift could power the growth of several key technologies for the renewable energy transition, including long-range electric cars and large-scale stationary applications for home utilization and industrial sites[3, 4].

To date, ceramics and polymers constitute the two most promising families of solid-state electrolyte materials [5]. Cubic garnet $Li_7La_3Zr_2O_{12}$ (LLZO) has attracted considerable interest among ceramics due to its high ionic conductivity and compatibility with metallic lithium [6, 7, 8]. Nonetheless, LLZO is brittle and provides poor intimate contact with the electrodes, resulting in high interfacial resistance, crack formation and dendrite growth [9, 10]. Alternatively, polymer electrolytes are more flexible and improve interfacial contact with the electrodes, while providing better mechanical stability during cycling. Poly(ethylene oxide) (PEO)-based polymer electrolytes are the most extensively studied and may be found in commercial batteries [11]. However, they fail to inhibit dendrite formation at high current densities, leading to short-circuit and battery failure [12, 13].

Composite solid-state electrolytes (CSSE) materials aim to combine the beneficial aspects from each family by embedding ceramic particles (the filler) within an ion-conducting polymer phase [14]. PEO(LiTFSI) polymeric complexes (LiTFSI = Li$^+$ bis(trifluoromethanesulfonyl) imide) incorporating LLZO particles have been proposed, with the hope that this filler reinforces the polymer matrix, decreases the polymer crystallinity and most critically, provides a high conductivity path for the Li$^+$ ions [15, 16, 17]. While the first two goals have been achieved with relative success using LLZO and other fillers, the latter has been elusive because of the high interfacial resistance between the polymer and garnet phases [18, 19, 20]. Therefore, ionic transport remains mostly confined to the polymer phase. Nonetheless, conductivity enhancement has been reported at relatively low LLZO contents ($10-20\%$ volume), and it is attributed to percolation effects arising from the presence of a highly conductive layer surrounding the filler particles [21, 22, 23, 18]. At a given volume fraction (which depends on the filler particle size), these layers overlap to form a spanning cluster through which the Li$^+$ ions can diffuse faster through the electrolyte. The nature of such layer is partially attributed to a loss of crystallinity in the polymer phase around the filler particles [24], which agrees with the fact that the enhancement is more pronounced below the melting temperature of PEO, T_m. However, this phenomenon also occurs above T_m, suggesting that additional mechanisms are at play [21]. The most often invoked one is related to the presence of space-charge effects (SCEs), i.e. the formation of an electric double layer, in which a Li$^+$ rich region develops in the vicinity of the garnet surface, and the ions are able to diffuse nearly unhindered by the presence of salt anions [25, 22, 23]. However, while crystallinity loss in CSSEs has been directly probed through x-ray diffraction[24], conductivity-enhancement due to SCEs is always deduced from indirect evidence. Zheng et al. [18] found that surface impurities may also lead to a Li$^+$-rich layer on the LLZO surface, enhancing the conductivity by releasing ions into the polymer phase. Villa et al. [26] showed that at equivalent volume fractions, PEO-based CSSEs incorporating LLZO were more highly conductive than those incorporating a passive (non-conducting) filler (Al$_2$O$_3$).

3

This indicates that physical effects may not be solely responsible for the conductivity enhancement, but that the specific surface chemistry of the garnet and its interactions with the polymer could have an influence.

Atomistic modelling of CSSEs is scarce and has focused almost exclusively on passive oxide fillers [27, 28]. Recently, we employed molecular dynamics (MD) and enhanced hybrid Monte Carlo techniques to simulate, for the first time, the Li^+ dynamics near the filler/polymer interface in LLZO:PEO(LiTFSI) CSSEs [29]. Our work automatically yielded the interfacial Li^+ distribution assumed in space-charge models [19] and showed that specific PEO - LLZO interactions lead to a long-range impact of the garnet surface on the Li^+ diffusivity. In addition, we unveiled the presence of a highly resistive, 0.4 nm thick Li^+ free layer, reminiscent of the Stern layer in the Gouy-Chapmann-Stern equations of the electric double layer [19]. However, we found this layer to originate from the inability of the polymer chains to fully coordinate the Li^+ ions very close to the LLZO surface.

Despite these exciting results, several crucial questions remain unanswered. First, we did not detect conductivity enhancement associated with the SCEs. One possibility is that such effects (or other enhancing mechanisms) may only arise when two or more particles are in close proximity. Second, we did not explain the high resistance to interfacial Li^+ exchange, which is essential to figure out effective strategies to minimize it. Finally, we hypothesized that above T_m, the overlap between garnet-bound polymer chains led to a significant decrease in the ionic conductivity with respect to that in free amorphous PEO. This hypothesis could adequately explain our experimental data and that from Zagorski et al. [17], but was not atomistically verified.

In this work, we tackle these open questions by simulating LLZO:PEO(LiTFSI) CSSEs under conditions of high polymer phase confinement. To do this, we combine the generalized shadow hybrid Monte Carlo method (GSHMC), MD simulations and umbrella sampling calculations. Recently, we demonstrated that GSHMC is a powerful tool to achieve equilibration in interfacial systems involving polymers [29], which often require multi-step strategies to reach full

4

chain relaxation [30, 31]. We examine the high temperature regime ($T = 450$ K), in which the polymer phase is fully amorphous and consider -OH terminated chains. The reasoning for focusing on amorphous PEO at 450 K is two-fold. Firstly, while in practice PEO is semicrystalline up to $T_m \sim 339 - 341$ K (i.e., at typical operating conditions) [17], the presence of inorganic filler particles plasticizes the surrounding polymer [25]. Moreover, Li^+ transport occurs primarily through the amorphous polymer pathways in between PEO crystallites, which means that the role of amorphous PEO in ionic transport is fundamental even below T_m [32]. Secondly, we have shown previously [29] that the mechanism of interfacial diffusion, the structure of the interface and the overall effect of the LLZO surface is qualitatively the same at 343 K and 450 K, although simulations at the former temperature require significantly longer production times.

First, we must define two important concepts: The *polymer shell* constitutes the thinnest layer enclosing all of the PEO chains bound to the LLZO surface, while the *rigidified layer* constitutes the region in which all available EO belongs to a bound PEO chain. Therefore, the polymer shell contains the rigidified layer. These two concepts will be considered in greater depth in the following sections.

In Section 3, we describe the LLZO:PEO(LiTFSI) simulation box and the impact of increasing polymer phase confinement on the distribution of Li^+ and $TFSI^-$ ions. We find a growing depletion of dissolved Li^+ in PEO(LiTFSI) as the garnet walls from adjacent LLZO particles approach each other, which is explained through the free energy calculations performed in Section 4. Despite the strong thermodynamic drive towards Li^+ uptake by the garnet, the presence of a rigidified polymer layer, explored in Section 5, induces a kinetic barrier that considerably slows down Li^+ adsorption by LLZO. Thus, any engineering effort to increase Li^+ interfacial exchange must simultaneously reduce the thickness of the rigidified polymer layer and the thermodynamic barrier to Li^+ transfer from the LLZO to the polymer. In Section 6, we discuss Li^+ diffusion in the polymer phase under strong confinement, providing atomistic evidence for the detrimental effect of overlapping bound polymer shells over Li^+ transport. Al-

5

though our simulations are all performed above T_m, Section 7 shows how our results can be exploited to explain the experimental variation of conductivity with LLZO content in LLZO:PEO(LiTFSI) CSSEs below T_m.

2. Methods

Non-bonded interactions for LLZO were modeled as a sum of Coulombic and Buckingham potentials, as repoted in our previous work [29]. On the other hand, the OPLS force-field [33] was employed to calculate bonded and non-bonded interactions of PEO chains, as well as the interatomic interactions between PEO and Li^+ ions [34]. Model parameters for interactions of $TFSI^-$ anions were taken from the work of Ködermmann et al. [35]. A scaling factor of 0.55 was, however, applied to the charge of N atoms to preserve electroneutrality in the LiTFSI molecules. In both cases, PEO and $TFSI^-$, interatomic interactions were well-defined by the Coulomb and Lennard-Jones (LJ) potentials, and the cross PEO/$TFSI^-$ interactions were calculated *via* the Lorenz-Berthelot mixing rules. This combination of force fields was validated previously by comparing with experimental conductivity data for several EO:Li ratios at 343 K and 358 K [29]. We reproduce such validation in Figure S1 of the SI for completeness. In addition, we provide the charges for the atoms in the polymer phase in Table S1.

Conversely, the PEO/LLZO and $TFSI^-$/LLZO cross parameters are not clearly defined, as the form of the potentials employed was substantially different. To calculate these cross terms, we adapted [29] the parametrization strategy by Lim [36] by reformulating the Buckingham-type potentials in a LJ form.

2.1. Simulation Setup

Dynamic calculations were performed through two simulation schemes: molecular dynamics (MD) and the generalized shadow hybrid Monte Carlo (GSHMC) method proposed by Akhmatskaya and Reich [37]. The GSHMC is a generalized

HMC method [38] where sampling is performed with respect to modified Hamiltonians, enhancing sampling efficiency by alternating short MD trajectories and stochastic Monte Carlo (MC) trial steps. While GSHMC has the advantage over MD as it rigorously controls temperature and samples more broadly due to its stochastic nature, it also preserves dynamical information and reaches high acceptance rates. GSHMC is included within the MultiHMC-GROMACS software code [39, 40, 41], which is an in-house modified version of the open-source MD package GROMACS 4.5.4 [42]. Tunnable input parameters of GSHMC were taken from previous work on polymer and LLZO electrolytes[29, 43, 44]: $L = 250$ (length of MD trajectories), $\Delta t = 2$ fs (time step), $\phi = 0.1$ (partial velocity update parameter).

We combined GSHMC with the two-stage-modified adaptive integration approach (MAIA)[41] specifically designed for modified HMC methods, which allowed an increased sampling performance without impacting the time step. In MD simulations, the standard velocity Verlet integrator has been applied with the time step of 2 fs.

Simulations were performed for polymer chains with $N = 10$ and 20 EO units at 450 K. All the initial configurations were generated with the Packmol[45] package. While GSHMC was used to efficiently equilibrate the initial configurations (up to 37 times faster than MD[29]) MD was employed for production runs. To stabilize the cubic garnet at the target temperature, we introduced Ga^{3+} (0.15 per formula unit) into the Li^+ sublattice of LLZO[25, 44]. The simulation boxes contained $3 \times 3 \times 3$ LLZO supercells (containing 1416 Li atoms, 648 La atoms, 432 Zr atoms, 2592 O atoms, and 32 Ga atoms), and a fixed number of LiTFSI molecules and PEO chains that ensured the target concentration EO:Li = 20 : 1[17] to be reproduced for the different gap thicknesses, Δ, where the polymer phase is confined. For $\Delta = 1$ nm, 2.5 nm, 5 nm, and 8 nm, we included 11, 24, 46, and 88 LiTFSI molecules, respectively. While the initial configuration of the LLZO garnet was obtained from a sampling technique applied in our recent works[43, 44, 29], the PEO and LiTFSI molecules were randomly distributed in the simulation box. Periodic boundary conditions

7

(PBCs) were applied in all directions. Van der Waals interactions were evaluated within a cut-off radius $r_{vdw} = 1.2$ nm, and Coulomb electrostatics were estimated with the smooth particle mesh Ewald method (PME) with a cut-off distance $r_c = 1.1$nm. Because periodicity also holds in the x direction and $2r_c$ is always below the cell size, the PME method is appropriate for the present system. The LLZO/PEO(LiTFSI) systems were equilibrated for 10 ns using GSHMC in the NVT ensemble. All the production runs, with a total simulation time of 150 ns, were carried out using MD in the NVT ensemble, where the average temperature was kept constant via a velocity rescaling thermostat (coupling time constant, $\tau_v = 0.1$ ps) at the specified target temperature $T = 450$ K. Bond lengths with H atoms were constrained using the LINCS algorithm[46].

Umbrella sampling (US) calculations[47] were employed to obtain the free energy profiles reported in Section 4. First, we randomly selected a Li^+ ion (Li*) from the garnet surface and performed a steered MD run perpendicularly to the interface (along the x axis) leaving all other coordinates unconstrained. Li* was slowly pulled at a rate of 0.5 nm ns^{-1} and with a spring constant k of 103.643 eV nm^2 (10^4 kJ mol^{-1}nm^{-2}) with respect to the garnet center of mass. The rationale behind this value of k will be explained later.

The US calculations were performed on the CSSE structure with $\Delta = 8$ nm and $N = 10$. We randomly selected three exposed Li^+-sites on the garnet surface. By *exposed* we mean that there are no coordinating oxygens beyond the location of the site that could hinder the extraction of the chosen Li^+ ion along a straight line parallel to the x-axis. If the Li^+ ion had to be extracted through a curved trajectory due to an oxygen obstructing its path, the free energy required would likely be higher than that calculated in this work.

21 US windows ($i = 0, ..., 20$) were set up at a distance $\delta x_i = \delta x_{i-1} + 0.05$ nm from the initial position of Li* on the garnet surface ($\delta x_0 = 0$). The initial configuration for each window was taken from selected snapshots generated during the steered MD runs. 15 to 35 ns NVT MD simulation runs were carried out at each window, with the first 5 ns discarded to allow for energy, temperature and polymer radius of gyration equilibration. The windows were finally combined

8

using the weighted histogram analysis method (WHAM).[47, 48] To restrain
Li* at each window, the spring constant k defined above was employed. We
found through trial and error that this value allowed for good overlap between
the umbrella histograms for the selected window separation, ensuring adequate
sampling. A typical histograms diagram is shown in Figure S5 of the SI, while
section S7 provides further details on the selection of k.

3. The LLZO:PEO(LiTFSI) CSSE

Figure 1 depicts a snapshot of the simulation box for the LLZO:PEO(LiTFSI)
system upon equilibration. The polymer phase is confined between semi-infinite
LLZO particles, within a gap of thickness Δ. This configuration mimics the in-
terstitial space between "large" garnet particles at a volume fraction $\frac{\pi}{6}(\Delta/d_p +$
$1)^{-3}$ (see Section S3 in the SI for derivation). Here, "large" indicates that the
particle diameter d_p is much larger than the mean length of the relaxed polymer
chains, l_p. The boundaries are kept periodic in all directions. Although heavy
La^{3+} and Zr^{4+} ions preserve their original lattice positions, an amorphous 4
Å layer of Li^+ ions *originating* from the garnet phase, Li_g^+, arises upon thermal-
ization of the polymer/garnet interface. Such a layer is highlighted in Figure 1 by
the blue bands on each interface, and its nature has been discussed elsewhere[29].
However, we remark that the two available LLZO surfaces differ in their ter-
minations, a necessary requirement to maintain electroneutrality. This leads to
variations in the distribution of Li^+ sites within the amorphous layer, as shown
in the two panels to the left of figure 1. Ultimately, this induces differences in
the distribution of PEO atoms and salt ions near the garnet/polymer interfaces.
Nonetheless, these differences do not affect the main conclusions of the present
work.

Figure 2 depicts the number density profiles, ρ_i, for selected atoms in the
CSSE, for $1 < \Delta < 8$ nm and $N = 10$, where N is the number of EO units in
the polymer (the curves for $N = 20$ are essentially identical, and can be found
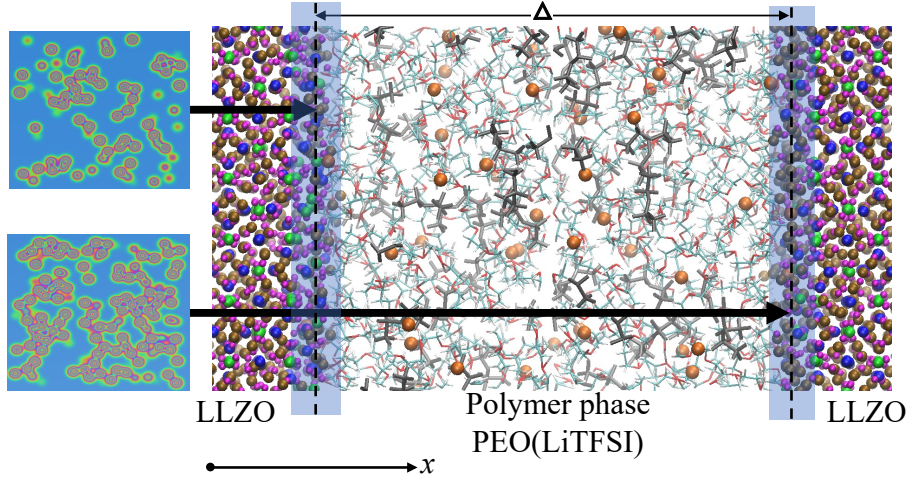in Figure S3 of the SI). $\Delta = 8$ nm (1 nm), is equivalent to having uniformly dis-

9

Figure 1: The simulation box for the LLZO:PEO(LiTFSI) system. The polymer phase (PEO + LiTFSI) is confined within the LLZO walls with a tickness Δ. The boundaries are periodic in all directions. Brown, magenta, bright green, blue and white spheres within the garnet correspond to Li_g^+ (Li^+ ions originating in the LLZO), O^{2-}, Zr^{4+}, La^{3+} and Ga^{3+} ions, respectively. Li_p^+ ions (Li^+ ions originating in the polymer phase) are shown in orange, while PEO and LiTFSI correspond to the -red-blue- and gray chains, respectively. The panels to the left represent the two-dimensional projection of the density distribution of Li_g^+ on the dashed lines within the amorphous interface layers.

persed 1 μm particles at a volume fraction $\omega = 41\%$ (51%), or 50 nm particles at $\omega = 33\%$ (49%). While these garnet contents are high, the present simulations

235 offer the possibility of analyzing what happens when the polymer shells surrounding each particle[49, 50, 23] overlap. Such overlapping has been reported to lead to room-temperature conductivity spikes at $10 < \omega < 20\%$ [21, 23]. The distribution of Li_g^+ appears to differ significantly between the panels of Figure 2. However, this effect arises due to the different scales of the x-axis. Figure S2 in

240 the SI depicts Li_g^+ for $\Delta = 1, 2.5$ and 5 nm, but removing the gap confining the polymer phase and putting all of the curves within the same scale. While the magnitude of the peaks and valleys in $\rho_{Li_g^+}(x)$ differ, their locations and relative sizes largely converge. The differences in magnitude can be attributed to the fact that, within our simulation timescales, the theoretical occupancies for each

site in the Li sublattice are not uniformly reached. In addition, variations of Δ lead to changes in the distribution of polymer and ions near the interface, which in turn yields variations in the distribution of Li_g^+ at the garnet surface.
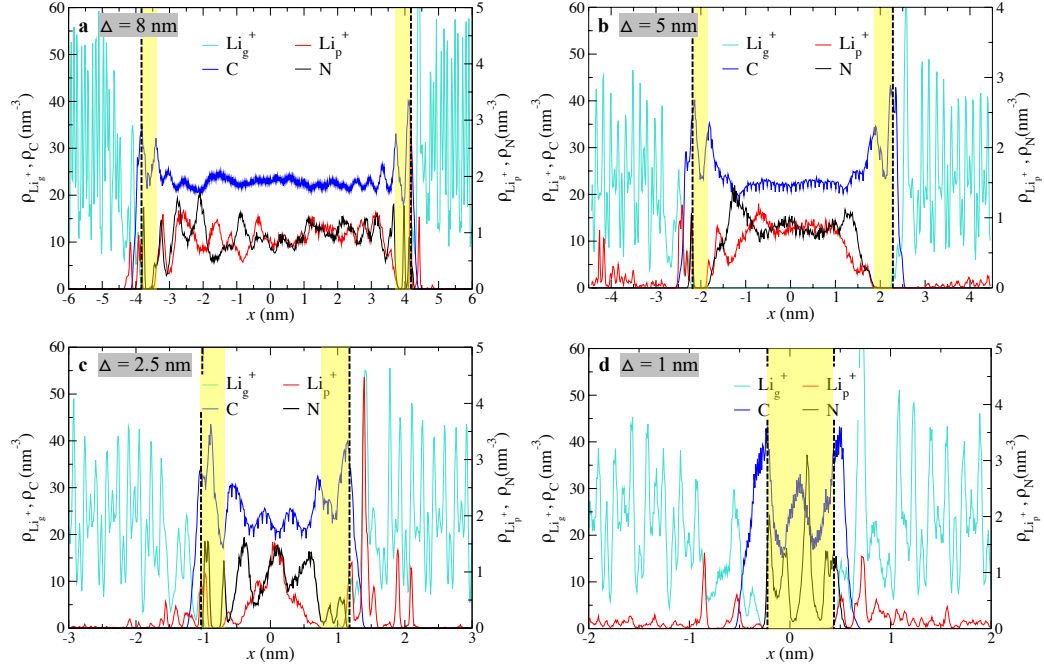

Figure 2: Density profiles for selected atoms in the CSSE: C atoms from PEO (blue), N atoms from the TFSI$^-$ anions (black), Li$^+$ ions *originating* in the garnet phase, Li_g^+ (cyan), and the polymer phase, Li_p^+ (red). The curves were extracted at 450 K, for $N = 10$ and **a** $\Delta = 8$ nm, **b** $\Delta = 5$ nm, **c** $\Delta = 2.5$ nm, and **d** $\Delta = 1$ nm. The yellow bands represent Li$^+$ free layers on the polymer side of the interface. The dashed lines indicate the limits of the garnet surfaces.

The yellow bands in Figures 2a-d highlight Li$^+$ free layers on the polymer side of the interface, akin to the Stern layer in the Gouy-Chapmann-Stern model [19]. Recent simulations found this layer to have a thickness $\delta \sim 4$ Å for large values of Δ [29]. While this condition still holds for $\Delta = 2.5, 5$ and 8 nm, we find that $\delta = \Delta$ for $\Delta = 1$ nm. That is, all Li_p^+ is transferred from the polymer to the garnet phase. Moreover, we observe that the fraction of transferred Li_p^+ decreases with increasing Δ, even though the initial EO:Li_p^+ ratios and polymer densities are the same for all systems.

The distributions of Li_p^+ and N atoms appear correlated for $\Delta = 5$ and 8 nm. However, such correlation is lost for lower values of Δ. Thus, the observed behavior does not result from interactions between the garnet and salt anion, but is more likely related to changes in the distribution of polymer under severe confinement. However, simply inspecting ρ_C in Figure 2 is not enough to extract any meaningful relationship with $\rho_{Li_p^+}$. In the following sections, we will explain the origin of the above observations, and describe how they may relate to the experimental percolation effects.

4. Li^+ diffusion energy barriers at the garnet:polymer interface

Figures 2a-d shows that the density profile of Li_g^+ (cyan curve) is confined to the location of the garnet, never crossing into the polymer phase. This indicates that the transfer of Li^+ from the garnet to the polymer is a rare event, beyond the timescales amenable to our MD simulations (100 ns). Because of the heterogeneous nature of the garnet surface, and the exceedingly large number of degrees of freedom available in the polymer phase, it is rather challenging to predict the average energy barrier associated with the transfer of a Li^+ ion from LLZO to PEO(LiTFSI) using only atomistic tools. However, by calculating the free energy profile, $F(x^*)$, for individual Li^+ ions along viable reaction coordinates, we can qualitatively elucidate the mechanistic origin of the density profiles, $\rho_{Li_p^+}$ and $\rho_{Li_g^+}$, depicted in Figure 2. Here, coordinate x^* denotes distance from the garnet surface.

First, we randomly selected a Li^+ ion (Li^*) from the garnet surface and performed a steered MD run perpendicularly to the interface. Subsequently, umbrella sampling (US) calculations were performed by running constrained MD runs at selected windows along the steered MD trajectory (we chose a window every 0.05 nm). $F(x^*)$ was estimated through the Weighted Histogram Analysis Method (details and parameters for these calculations can be found in subsection 2.1).

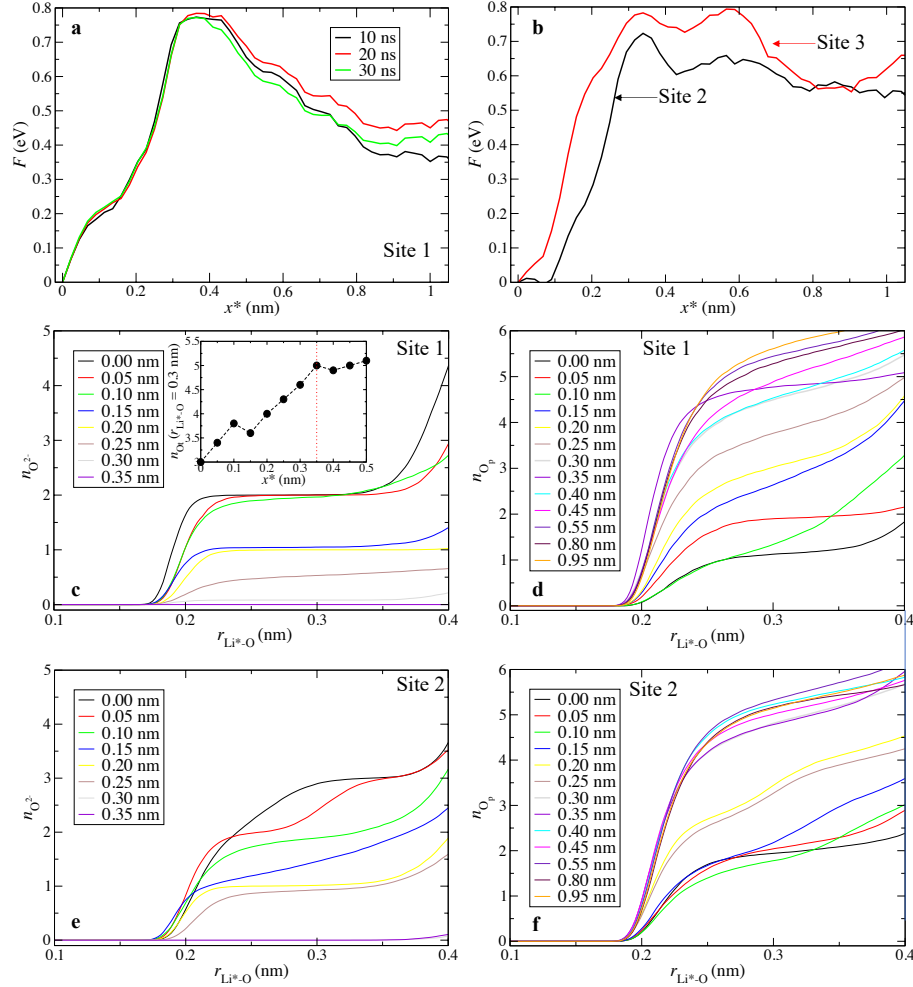Figure 3a shows $F(x^*)$ for the extraction of a Li^+ ion from a randomly chosen

12

Figure 3: **a** Free energy profile, $F(x^*)$, associated with the extraction of a selected Li^+ ion, Li^*, from the garnet surface at 450 K and for $\Delta = 8$ nm, obtained through umbrella sampling (US) calculations. x^* denotes distance from the garnet surface. Windows in the US scheme were separated by 0.05 nm. The profiles for three simulation lengths per window ($t_w = 10$, 20, and 30 ns) are shown. **b** $F(x^*)$ associated with the extraction of selected Li^+ ions at two other randomly selected surface Li-sites ($t_w = 10$ ns). **c, d** Average number of garnet oxygens, $n_{O^{-2}}$, and polymer oxygens, n_{O_p}, respectively, within a shell of diameter r_{Li^*-O} around the Li^+ extracted from site 1, at several values of x^*. Inset: total coordination $n_{Ot} = n_{O^{2-}}|_{r_{Li^*-O}=0.3 \text{ nm}} + n_{O_p}|_{r_{Li^*-O}=0.3 \text{ nm}}$. **e, f** $n_{O^{-2}}$, and n_{O_p} within a shell of diameter r_{Li^*-O} around the Li^+ extracted from site 2 at several values of x^*.

13

surface site (designated site 1) at 450 K and for $\Delta = 8$ nm. The MD simulations at each window were run for time spans, t_w, of 10, 20 and 30 ns. Interestingly, the free energy curves tend to separate as x^* increases when $x^* > 0.35$ nm, but are nearly identical for $x^* < 0.35$ nm. The differences for $x^* > 0.35$ nm are indicative that $t_w = 30$ ns may be too short to accurately define $F(x^*)$ far from the interface where free polymer becomes available, while $t_w = 10$ ns is reliable for $x^* < 0.35$ nm. Figure 3b shows $F(x^*)$ for the extraction of a Li$^+$ ion from two additional surface sites (sites 2 and 3) at the same conditions described before, and for $t_w = 10$ ns. While the shape of $F(x^*)$ differs for each site, the peak energy in all cases is between 0.7 and 0.8 eV, and is located at $x^* \sim 0.35$ nm. This indicates that the work required for a Li$^+$ ion to traverse the Li$^+$ free layer is within this energy range, even though the curves themselves differ significantly as a consequence of the large variation in available atomistic and molecular environments.

The results above can be rationalized as follows. It is well understood that Li$^+$ ions are coordinated by a shell of ~ 5 polymer oxygens in amorphous PEO [51, 30, 29, 52]. These oxygens are commonly associated with a single polymer chain [52]. Long-range diffusion occurs through Li$^+$ hopping between coordination shells in adjacent chains, and thus is highly correlated with the ability of the PEO chains to quickly fold and "surround" the diffusing ion [30]. For $x^* > 0.35$ nm, polymer segments are far enough from the garnet surface to freely fold and form a coordination shell around Li*. As x^* and t_w increase, the hopping likelihood within a given window increases, producing the divergence in $F(x^*)$ observed in Figure 3a.

For $x^* < 0.35$ nm, the oxygen coordination shell is incomplete. To illustrate this, Figures 3c and 3d depict the cumulative radial distribution function

$$n_\text{O}(r) = 4\pi\bar{\rho}_\text{O} \int_0^r r'^2 g_{\text{O}-\text{Li}^*}(r')dr', \tag{1}$$

for the Li* from site 1 and both O $=$ O^{2-} (oxygens from the garnet) and O $=$ O$_p$ (oxygens from the polymer phase). Here, $\bar{\rho}_\text{O}$ is the average density of O atoms and $g_{\text{O}-\text{Li}^*}(r)$ the radial distribution function for the O $-$ Li* pair.

14

At $x^* = 0$, Li* is coordinated in average by two O^{2-} atoms and one O_p atom within a 0.3 nm shell. Thus, Li* is undercoordinated with respect to both the polymer and the garnet phase. In spite of this, diffusion towards the polymer is strongly penalized, given the rapid increase in $F(0 < x* < 0.35 \text{nm})$ depicted in Figure 3a. To explain this, we must recall that the coordination shell around a Li^+ atom is considerably tighter in the LLZO lattice than in bulk PEO. Indeed, Figure 3c shows that the O^{2-} coordination shell has an average radius of 0.22 nm at $x* = 0$, compared to the 0.3 nm shell formed by the O_p atom (Figure 3d). In addition, electrostatic effects generate vacancy-rich bands near the LLZO surface [8, 19, 23]. As a consequence, diffusion towards the garnet bulk is significantly more likely than towards the polymer phase.

From $x = 0$ to $x = 0.35$ nm, $n_{O^{2-}}|_{r=0.3 \text{ nm}}$ decreases to 0, while $n_{O_p}|_{r=0.3 \text{ nm}}$ increases to 4.8. The inset in Figure 3c shows that the total oxygen coordination ($n_{Ot} = n_{O^{2-}}|_{r=0.3 \text{ nm}} + n_{O_p}|_{r=0.3 \text{ nm}}$) plateaus at $x^* = 0.35$ nm. Therefore, the Li^+ extraction barrier is the result of breaking the tight shell of garnet oxygens around Li* and transitioning to complete polymer coordination. At $x^* \sim 0.35$ nm, the electrostatic effect of the garnet oxygens is overcome by the interactions with O_p atoms. Nonetheless, it is costly for bound polymer chains to acquire configurations under which the Li* ion can be fully coordinated. For $x^* >> 0.35$ nm, polymer chains and $TFSI^-$ ions that are not bound to the garnet can now form a coordination shell around Li*, lowering the entropic cost and reducing $F(x^*)$ (more significantly so for site 1 within the simulated t_w values). Figure 4 schematically illustrate the evolution of the Li* extraction process.

The plots corresponding to $n_{O^{2-}}$ and n_{O_p} for the Li* from site 2 are shown in Figures 3e and f. Clearly, the local environments of sites 1 and 2 differ. For instance, $n_{O^{2-}}|_{r=0.3 \text{ nm}} \sim 3$ nm for site 2 (comparing the curves for $x^* = 0$ and $x^* = 0.05$ nm in Figures 3e reveals, however, that only 2 of the 3 O^{2-} ions are tightly bound to Li*; i.e., at an average distance of 0.22 nm). Even though these differences lead to substantial discrepancies in the shape of $F(x^*)$ for sites 1 and 2, similar results are obtained regarding the location and magnitude of the free energy peak. However, a key question remains unanswered: given

15

that $F(x^* > 0.35$ nm$) > F(0)$ up to $x^* = 1$ nm for all of the examined sites, why are there no more Li_p^+ ions transferring from the polymer to the garnet phase? In particular, $F(x^*)$ decreases very slightly within $0.35 < x^* < 1$ nm for Li* from sites 2 and 3, suggesting that such a transfer should occur quickly whenever these sites are available. Yet, the concentration of Li_p^+ in the garnet is insignificant for $\Delta = 8$ nm (see Figure 2a). The reason is not thermodynamic, but kinetic, and is described in the following section.
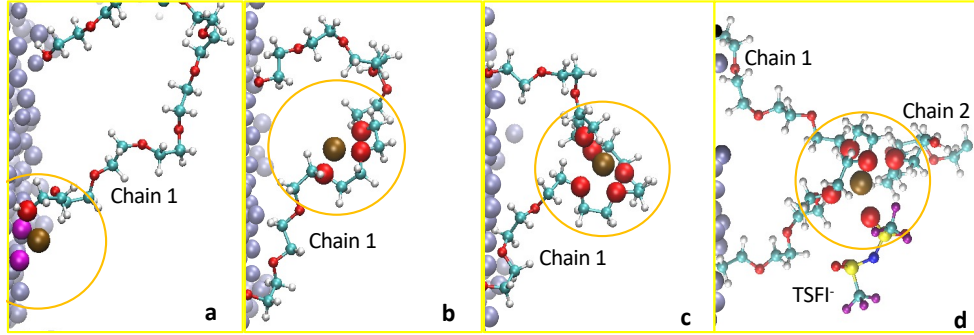

Figure 4: Selected snapshots depicting the evolution of a Li^+ ion, Li* (brown sphere), extracted from the garnet. **a** At $x^* = 0$, Li* is (under)coordinated by 2 O^{2-} ions (magenta sphere) and one O_p atom (large red sphere). **b** At $x^* = 0.3$ nm, Li* is coordinated by 3 O_p atoms from a single bound chain (chain 1). **c** At $x^* = 0.38$ nm, Li* is fully coordinated by 5 O_p atoms from chain 1. **d** At $x^* = 0.5$ nm, Li* is simultaneously coordinated by chain 1, chain 2 (not bound) and a free TSFI$^-$ anion, reducing the entropic cost of Li* coordination

5. Effect of rigidified polymer layer

The formation of a rigidified layer of polymer at the interface, due to attractive interactions between the polymer and filler promoted by stronger polymer-filler interaction compared to polymer-polymer interaction is a well-known problem in mixed matrix membranes for molecular sieving [53, 49, 54]. While its presence was reported in CSSEs incorporating passive fillers and amorphous PEO [27, 52], only recently was it theoretically investigated on CSSEs involving active fillers [29].
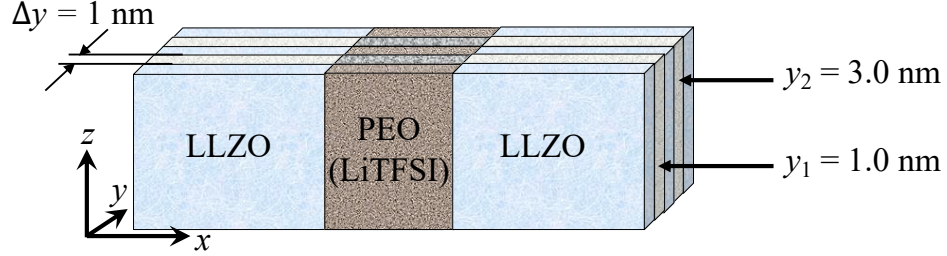
16

Figure 5: Density profiles $\rho(x)$ in Figure 6 are measured within slabs of thickness $\Delta y = 1$ nm centered at $y_1 = 1$ nm and $y_2 = 3$ nm.

The impact of the rigidified layer on interfacial transport can be further understood through the equilibrium density profiles. However, we found that considering the entire thickness of simulation box was insufficiently clear (see Section S5 in the SI for further details). Thus, we examined the density profiles within two slabs of thickness $\Delta y = 1$ nm centered at $y_1 = 1$ nm and $y_2 = 3$ nm, as schematically shown in Figure 5. The resulting density profiles are shown in Figure 6. The solid lines represent the densities of C (blue) and O_p (green) atoms from bound PEO chains only, while the dotted lines represent the densities of C and O_p for both free and bound chains. The regions where these lines coincide correspond to the rigidified polymer layers: in this region, all C/O_p atoms belong to bound chains, i.e., there are no segments of free chains available. We have highlighted the rigidified layers in yellow. In practice, they were identified as the areas in which the dashed and solid lines differ by less than 1 %.

Figures 6a-d show that, for $\Delta = 5$ nm, the Li_p^+ density profiles (red line) vanish within the yellow regions. Thus, the rigidified layer matches almost exactly the Li^+ free layer. The present result shows that free PEO chains are significantly better at stabilizing Li_p^+ ions than bound PEO. The reason behind it is associated with the higher flexibility of the free chains: beyond the rigidified layer, it is relatively easy for one (or more) free chain(s) in the vicinity of a Li_p^+ ion to quickly and effectively rearrange to form a stabilizing oxygen
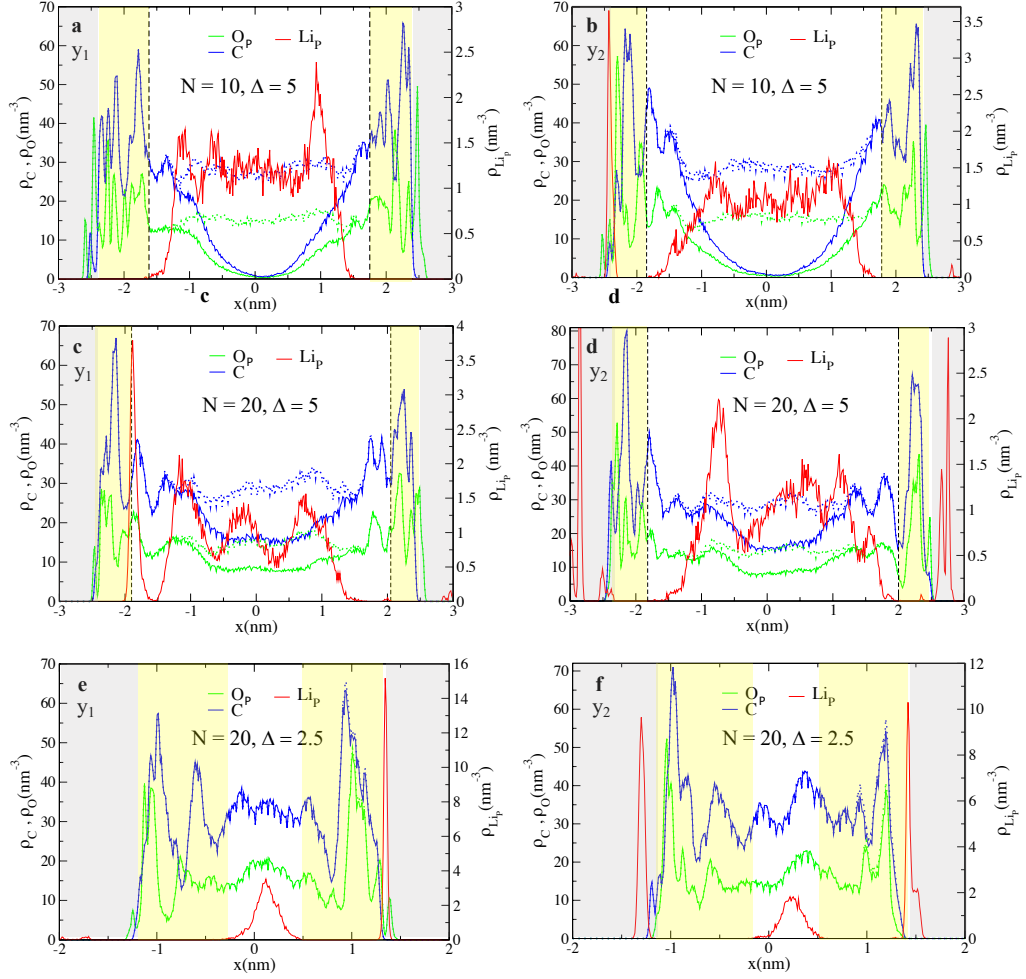
17

Figure 6: Density profiles $\rho_X(x)$ for $X = \text{Li}_p^+$, C and O_p and within slabs of thickness 1 nm in the y direction, centered at $y_1 = 1$ nm and $y_2 = 3$ nm (see Figure 5). The solid blue (green) line represents C (O_p) atoms from bound PEO chains, while the dotted blue (green) line represents C (O_p) atoms from all chains. The dashed vertical lines designate the lowest and highest x values at which corresponding solid and dotted lines merge. The yellow bands indicate the rigidified layer (where all available C and O_p belongs to a bound chain). The gray areas indicate the location of the garnet. The following configurations were examined: **a** $N = 10$, $\Delta = 5$ nm (centered at y_1). **b** $N = 10$, $\Delta = 5$ nm (centered at y_2). **c** $N = 20$, $\Delta = 5$ nm (centered at y_1). **d** $N = 20$, $\Delta = 5$ nm (centered at y_2). **e** $N = 20$, $\Delta = 2.5$ nm (centered at y_1). **f** $N = 20$, $\Delta = 2.5$ nm (centered at y_2).

18

coordination shell. We also note that the the overlap between polymer shells observed in Figures 6c,d ($\Delta = 5$ nm, $N = 20$) is much more significant than in Figures 6a,b ($\Delta = 5$ nm, $N = 10$). This results in a greater heterogeneity of polymer mobilities within the central region in Figures 6c,d, leading in turn to greater heterogeneity in $\rho_{\mathrm{Li}_p^+}$.

The thickness of the Li$^+$ free layer (defined by the thickness of the yellow bands) varies between 0.5 and 0.7 nm in Figures 6a and b, and 0.4 and 0.6 nm in Figures 6c and d. Nonetheless, its boundary is far from $x^* = 0.35$ nm, where the peak in $F(x^*)$ is located. That is, in order to make use of the downhill path in the free energy profile to reach the garnet surface, the Li$_p^+$ must first penetrate the rigidified layer. We can qualitatively visualize this by considering the scenario in which the Li$_p^+$ ion in Figure 4d evolves towards the configuration shown in Figure 4c: because Chain 2 is significantly more flexible than Chain 1, it can quickly "shuffle" around to capture Li$_p^+$ within a coordination shell, never giving Chain 1 enough time to form a "receiving" coordination shell to which Li$_p^+$ can hop into. Therefore, the rate at which Li$_p^+$ ions are adsorbed by LLZO is significantly slowed down due to the poor kinetics of the bound polymer, despite the considerable thermodynamic benefit. As a matter of fact, a large fraction of the Li$_p^+$ ions that were adsorbed by the garnet in our simulations were located, at $t = 0$, within the rigidified layer. We note that these conclusions apply for $\Delta \geq 5$ nm and with $N \leq 20$, when free polymer is available. However, we can assume that for smaller Δ and/or sufficiently large N, no free chains will remain. This situation is akin to that shown in Figures 6e and f.

For $\Delta = 2.5$ nm and $N = 20$, all polymer chains are bound to the garnet (Figures 6e,f). In the absence of free chains, any Li$_p^+$ remaining in the polymer phase must be confined in the central region, at least 0.35 nm away from either surface (as deduced from Figures 3a,b). At an equal distance from each surface one would expect the polymer to be most mobile, that explains the central peak in $\rho_{\mathrm{Li}_p^+}$. In fact, we have estimated that each Li$_p^+$ in the polymer phase is coordinated by an average of two different PEO chains at any given time. Thus,

19

the peak in $\rho_{\mathrm{Li}_p^+}$ near $x = 0$ corresponds to lithium ions that are "trapped" in coordination shells from polymer chains bound to opposite garnet surfaces.

Figures 6e,f also reveal significant adsorption peaks in $\rho_{\mathrm{Li}_p^+}$, 3 - 5 times more intense than those in Figures 6a - d. Moreover, the Li^+ free layer is 0.8 - 1 nm thick. This can be explained by noting that, under such degree of confinement, it will be significantly easier for Li_p^+ ions to find the downhill path in the free energy landscape towards the garnet surface. Indeed, in the most extreme confinement illustrated in Figure 2d for $\Delta = 1.0$ nm, not a single Li_p^+ is left in the polymer phase. We note that $\Delta = 2.5$ nm and $\Delta = 1.0$ correspond to large volume fractions, which are associated with low conductivity and brittleness [17]. However, we will use these scenarios of extreme confinement to show what happens to Li^+ diffusion when bound polymer shells around filler particles are close enough to overlap.
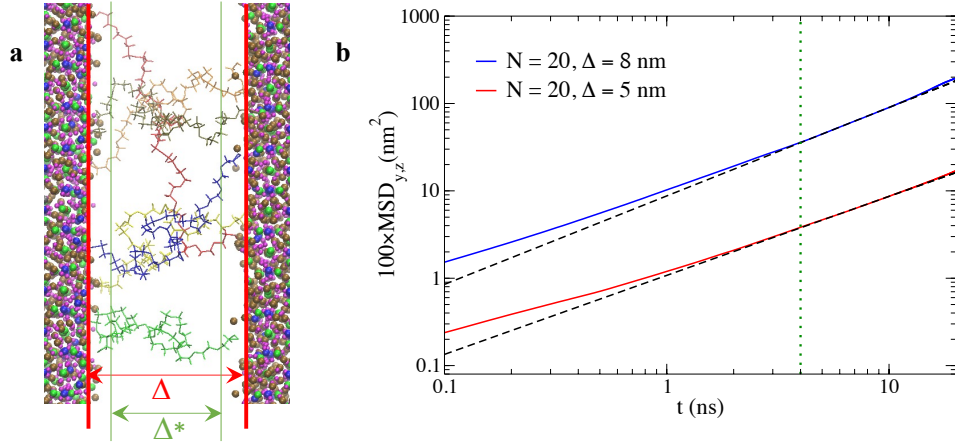

Figure 7: **a** When large garnet surfaces are sufficiently close ($\Delta \sim l_p$ and $l_p/d_p \ll 1$), individual polymer chains may interact with both interfaces as shown in the figure (free polymer chains or those bound to only one interface are not shown for clarity). The diffusivities are estimated within a region Δ^* at least 0.8 nm away from the garnet surfaces, with the goal of avoiding the rigidified polymer layers and the adsorption field from the LLZO. **b** log-log plot of the mean square displacement for Li_p^+ ions within Δ^*, at 450 K, and for systems with $N = 20$ and both $\Delta = 5$ and 8 nm. Past the vertical dotted line, the slope of the curves is approximately one.

20

6. Li$^+$ diffusion under confinement

In this section, we investigate Li$^+$ diffusion in the polymer phase under strong polymer confinement ($\Delta \sim l_p$ and $l_p/d_p << 1$, where l_p is the mean end-to-end distance of the PEO chains and d_p the particle diameter). Li$^+$ diffusion in the x direction is anomalous, due to the boundaries imposed by the garnet and the rigidified polymer layer. Thus, we focus on the diffusivity, D, in the $y - z$ plane, following the formulation proposed by Liu et al. [55] for lateral diffusion near surfaces (a brief summary can be found in Section S6 of the SI). To avoid the Li$^+$ free layer, we measure D within a region Δ^* at least 0.8 nm from the garnet surface (Figure 7a).
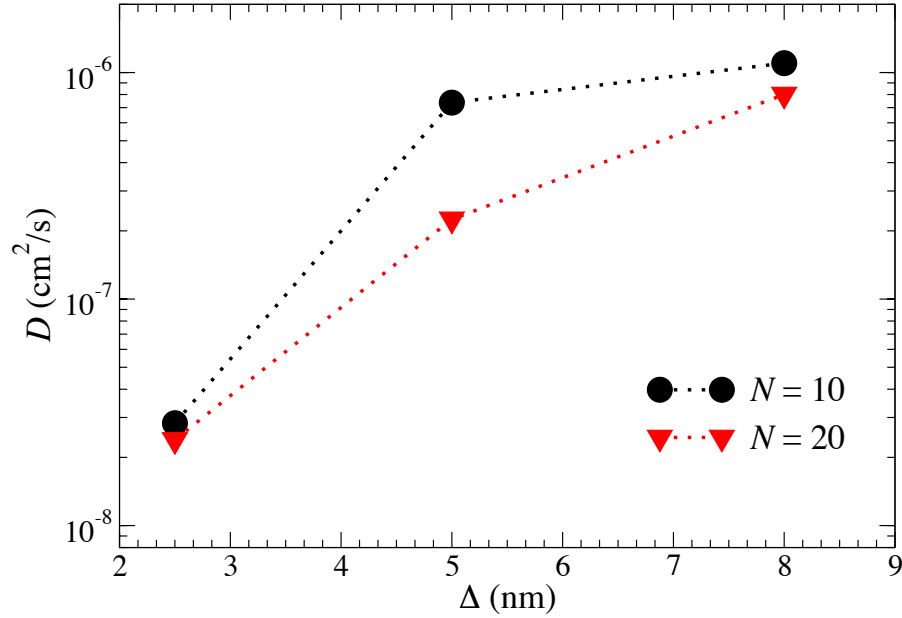

Figure 8: Diffusion coefficient, D, as a function of Δ, at 450 K and for PEO chains with $N = 10$ and $N = 20$.

Figure 7b depicts the mean square displacement in the $y-z$ plane, MSD$_{y,z}(t)$, for systems having $N = 20$, and $\Delta = 5$ and 8 nm at 450 K. The slope of the curves reaches unity at ~ 4 ns, indicating Fickian diffusion. Therefore, D can be

21

estimated for this study through Einstein's diffusion equation using the appropriate modifications to account for finite residence times [55]. The $\mathrm{MSD}_{y,z}(t)$ curves for all other investigated systems follow approximately the same behavior, although for $\Delta = 2.5$ nm Fickian diffusion is only registered after ~ 20 ns. There are clear differences in $\mathrm{MSD}_{y,z}(t)$ between $\Delta = 8$ nm and $\Delta = 5$ nm, despite the polymer length being kept constant. Below, we explain how such differences originate from the overlapping of polymer shells bound to opposing surfaces.

Previous experiments and simulations studies[30, 56] showed that the Li$^+$ diffusivity decreases with N by a factor of 2-3 for $20 < N < 100$ in bulk PEO(LiTFSI), and plateaus thereafter. Interestingly, Figure 8 reveals that although the ratio $r_D = D(N = 10)/D(N = 20)$ is always above unity (as expected), its magnitude is non monotonically dependent on Δ. While $r_D = 1.1$ for $\Delta = 2.5$ nm and 1.3 for $\Delta = 8$ nm, it raises to 4.5 for $\Delta = 5$ nm. To explain this behavior, let us recall that the "polymer shell" of a given surface correspond to the layer with minimum average thickness containing all the polymer chains bound to that surface. The rigidified layer, comprising the region in which "all" available polymer is physically bound to the garnet is part of the polymer shell. In fact, the polymer shell can be significantly thicker than the rigidified layer (the thickness of the polymer shell is $\sim N^{\frac{3}{5}}$ according to Lee et al.[57]).

Figure 9 illustrates the number density profiles for oxygen (O$_p$) and carbon (C) atoms from PEO chains bound to the garnet surfaces, for $\Delta = 2.5, 5.0,$ and 8.0 nm and for $N = 10$ and 20. We separate the profiles associated with the left and right interfaces, allowing us to visualize the thickness of the polymer shells for each garnet surface. Figures 9a,b indicate that for $\Delta = 2.5$ nm, the polymer shells from each surface largely overlap for both $N = 10$ and 20. In either cases, D is about two orders of magnitude below the bulk diffusivity of Li$^+$ in bulk PEO(LiTFSI) ($D_{\mathrm{Bulk}} = 3.3 \times 10^{-6}$ cm^2/s (2.1×10^{-6} cm^2/s) for $N = 10$ (20) at 450 K)[29]. Conversely, Figures 9e,f reveal that for $\Delta = 8.0$ nm, the polymer shells from each surface do not interact, and $D \sim 0.3 D_{\mathrm{Bulk}}$ regardless of N. Yet, the r_D values for $\Delta = 8.0$ nm and $\Delta = 2.5$ nm remain very close. Moreover, for
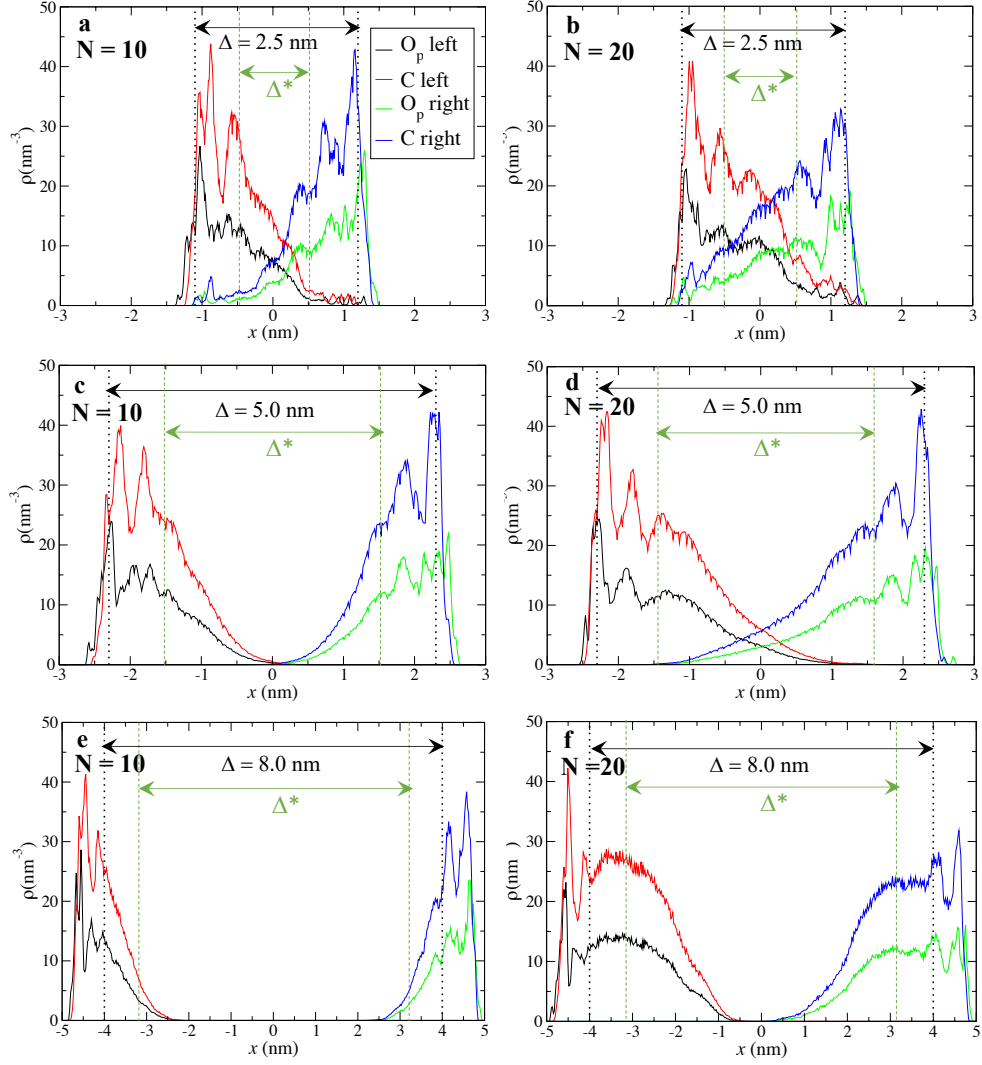
22

Figure 9: Density profiles of oxygen (O_p) and carbon (C) atoms from PEO chains bound to the garnet surface, at 450 K and for $N = 10$ and 20 at $\Delta = 2.5, 5.0, 8.0$ nm (Legend for all panels is available in panel **a**). Δ^* represents the region within which the values of D in Figure 8 were calculated. We disaggregate the profiles corresponding to chains bound to the left and right surfaces. The polymer shells from each side interpenetrate in **a**, **b** and **d**, impacting Li^+ diffusion.

$\Delta = 5.0$ nm, there is polymer shell overlapping when $N = 20$ (Figures 9d) and

no overlapping when $N = 10$ (Figures 9c), which produces a large $r_D = 4.5$. In previous work [29], we hypothesized that overlapping of the polymer shells from adjacent particles was responsible for the pronounced drop in Li$^+$ conductivity experimentally observed at high volume fractions ($\omega \sim 45\%$ for particles 1 μm in diameter and 10^6 g/mol PEO)[17]. While mechanical measurements and particle packing arguments supported this hypothesis, no atomistic evidence was provided at the time. The present results constitute definitive atomistic confirmation: overlapping of polymer shells leads to a dramatic reduction in the Li$^+$ diffusivity (by a factor of 4.5 in our case). As a consequence, a percolation-like drop in the ionic conductivity should occur when the "filler + polymer shell" pseudo-particles overcome random close packing[29], forcing all Li$^+$ ions through trajectories along the shells.

The segmental mobility of the polymer chains can be characterized by the autocorrelation function for the C–O–C–C dihedrals, $C_{\phi\phi}$: [58, 27]

$$C_{\phi\phi}(t) = \frac{\langle cos\phi(t)cos\phi(0)\rangle - \langle cos\phi(0)\rangle^2}{\langle cos\phi(0)cos\phi(0)\rangle - \langle cos\phi(0)\rangle^2}. \tag{2}$$

Figure 10 depicts the decay of $C_{\phi\phi}$ for bound PEO chains at three combinations of Δ and N. The slowest decay (and hence the lowest segmental mobility) corresponds to $\{\Delta = 2.5$ nm, $N = 10\}$. This is expected, as a small fraction of these chains is able to reach the opposite wall (see Figure 9a). However, there is little difference between $C_{\phi\phi}$ for $\{\Delta = 5$ nm, $N = 20\}$, and $\{\Delta = 5$ nm, $N = 10\}$. This indicates that polymer shell overlapping does not reduce the Li$^+$ diffusivity by decreasing the mobility of the overlapping bound chains. Simply, there is less free polymer available in the overlap region at the given density, lowering the frequency of interchain jumps.

7. Impact of confinement on ionic conduction

Several authors have reported SCEs capable of enhancing the ionic conductivity σ (which is roughly proportional to D[29]) in CSSEs when the filler
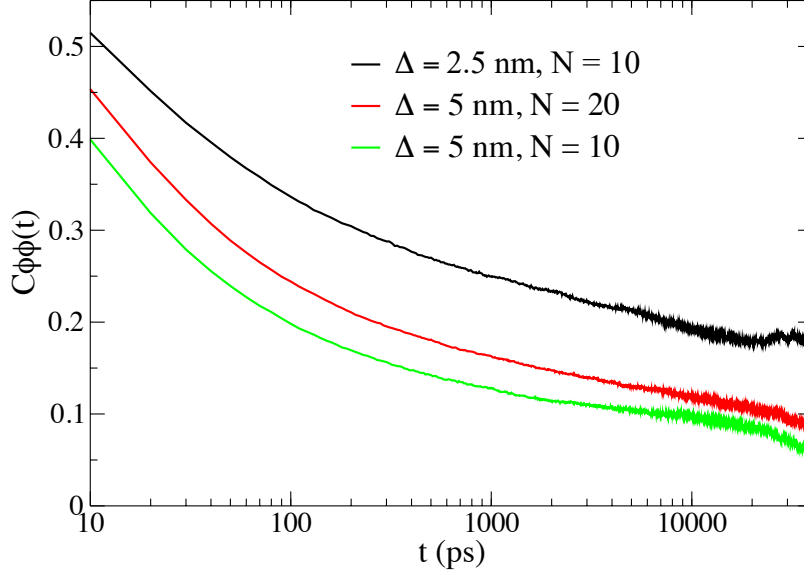
Figure 10: Variation of $C_{\phi\phi}$ with time for bound polymer chains at three different combinations of Δ and N.

particles are sufficiently close [60, 23]. We do not find evidence for such effects in our simulations. However, SCEs appear to manifest more strongly in CSSEs with small nanofillers (~ 10 nm), for which the conditions set out in this study ($\Delta \sim l_p$ and $l_p/d_p << 1$) are not met.

Conductivity enhancement below the PEO melting temperature T_m (~ 68 °C) may also be caused by loss of polymer crystallinity around the filler particles [61]. Because amorphous PEO is substantially more conductive than crystalline PEO, the formation of a spanning cluster of amorphous polymer leads to an increase in σ with ω for $T < T_m$, up to a critical value ω_c. This behavior has traditionally been modeled through effective medium theory (EMT) - based models [62, 24, 50]. EMT assumes the particles comprise an insulating core and a highly conductive shell, and predict reasonably well the variation of σ with ω in several CSSEs with passive fillers [62, 24]. Nonetheless, they also predict a dramatic decrease in conductivity for $\omega > \omega_c$, which is not observed in LLZO:PEO(LiTFSI). For instance, Zheng et al. [59] showed that σ decreases
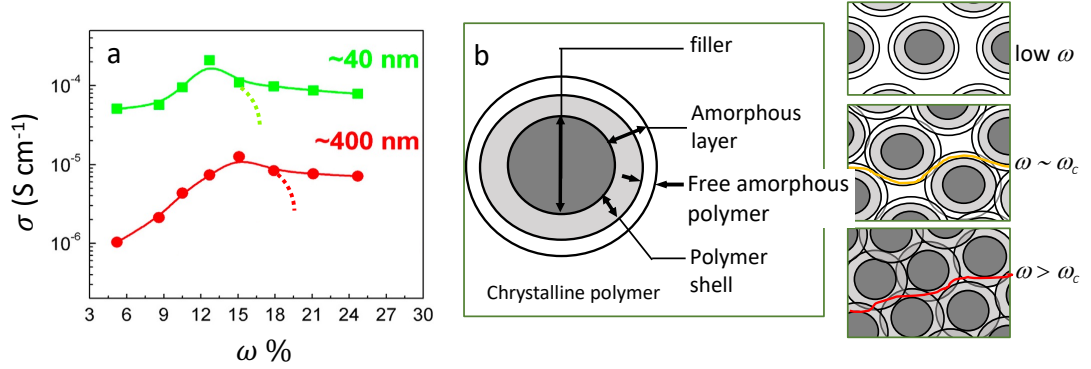
25

Figure 11: **a** The conductivity as a function of Ta-doped LLZO content for 40 and 400 nm particles in LLZO:PEO(LiTFSI) CSSEs at 30 °C. The solid line interpolates the experimental data, while the dotted line shows the typical curve shape obtained from core-shell EMT models. Adapted from Zheng et al.[59], Copyright Elsevier (2016). **b** Left panel: schematic of the proposed percolation process at $T < T_m$. The filler particles are surrounded by a layer of highly conducting amorphous polymer. The polymer shell (i.e., the collection of polymer chains that are physically bound to the filler particle) is contained within the amorphous layer. Right-top panel: at low ω, conduction through the crystalline phase dominates. middle-panel: at ω_c, a spanning cluster of overlapping amorphous layers arises, with minimal overlap between polymer shells. Bottom-panel: for $\omega > \omega_c$, polymer shells begin to overlap, reducing the conductivity at a relatively slow pace as ω increases.

slowly for $\omega > \omega_c$ in LLZO:PEO(LiTFSI) CSSEs with 40 and 400 nm particles at 30 °C, in contrast with typical EMT expectations (Figure 11a).

The results presented so far may shed some light into this behavior. We present in Figure 11b an alternative particle model, in which the filler parti-
cles are surrounded by a layer of amorphous polymer. The polymer shell has a conductivity σ_b and is contained within this amorphous layer, leaving a second outer layer of free amorphous polymer with conductivity σ_f. Assuming interfacial Li$^+$ exchange contributes negligibly to ionic conduction due to the high surface resistance [18, 19] and that $\sigma_f >> \sigma_b >> 10\sigma_c$ [29, 59], where σ_c is the
conductivity of crystalline PEO, we can explain the slow decay in the conductivity (σ) of the CSSE as follows: for $\omega < \omega_c$, the layers of free amorphous polymer begin to overlap as ω increases, leading to overall conductivity enhancement in

26

the CSSE. At $\omega = \omega_c$, a spanning cluster of free amorphous polymer forms that produces a maximum in σ. However, such a maximum is tempered by the overlapping of polymer shells, which was shown to negatively impact Li^+ diffusion. Increasing ω enhances the fraction of overlapping polymer shells, further reducing the conductivity while still allowing a relatively high ionic flow as compared to that in the crystalline polymer.

It has been found that at $\omega \sim 33\%$ a spanning cluster of LLZO particles may also arise, allowing Li^+ transport through the garnet phase [18]. This latter diffusion path is known to be hindered by high grain boundary resistances, but would still contribute to dampening the decline in the conductivity. Thus, the significant drop in $\sigma(T < T_m)$ predicted by several EMT models past ω_c may not occur in CSSEs with active fillers that can develop a bound polymer shell.

Additional quantitative work will be required to validate our double layer model, but it is a promising framework to uncover this intriguing phenomenon.

8. Conclusions

This work investigates the Li^+ spacial distribution and dynamics in LLZO:PEO(LiTFSI) CSSEs at conditions of high polymer confinement. Specifically, we focus on high temperature systems (450 K) and large filler particles ($\Delta \sim l_p$ and $l_p/d_p << 1$), in which the polymer phase is fully amorphous and the particles can be assumed to be semi infinite perpendicularly to the interface. By employing umbrella sampling calculations, we show that the free energy profile associated with the extraction of a Li^+ ion from the garnet surface is highly heterogeneous and may require very long MD runs at each window in the umbrella sampling scheme. However, the maximum free energy is surprisingly uniform at 0.7 - 0.8 eV for the three studied cases, and occurs ~ 0.35 nm from the garnet surface. Moreover, the free energy profile is non symmetric, suggesting a thermodynamic drive towards Li^+ adsorption into the garnet phase. We show that surface Li^+s are coordinated by a combination of polymer and garnet oxygens, with the latter forming a tighter shell. It is only beyond 0.35 nm from the garnet surface that

27

the polymer coordination shell reaches its typical bulk density of ~ 5 oxygens per Li^+, leading to a slight decrease in the free energy. We show that the thermodynamic trend towards Li^+ uptake by the garnet is counteracted by a kinetic effect: free polymer chains are significantly more mobile than garnet - bound chains. Hence they can quickly adapt to coordinate and stabilize incoming Li^+ ions. As a consequence, Li^+ jumps from a free chain to an adjacent bound chain are far less frequent than those to adjacent free chains, minimizing the actual amount of Li^+ reaching the LLZO surface. Only at very high garnet contents we predict Li^+ adsorption to be thermodynamically controlled, but such contents are, in general, of no practical interest.

We also demonstrate that the overlapping polymer shells lead to a decrease in Li^+ diffusivity within the interstitial space. This was originally hypothesized in our previous work [29] but remained untested. In addition, we fully discard conductivity-enhancing SCEs at the specific conditions studied here. They may still be present in CSSEs incorporating small nanoparticles, at lower temperatures or with methyl-terminated PEO chains. Moreover, additional conditions may be required at the interface for these effects to manifest (such as residual Li_2ClO_3 impurities, which is largely present in typical synthesis approaches [18, 20]).

Understanding Li^+ diffusion in LLZO:PEO(LiTFSI) CSSEs above the polymer melting point, T_m, and at conditions of high polymer confinement may still provide valuable insights to interpret the variation of ionic conductivity, σ, with volume fraction, ω, below T_m. This is because filler particles are thought to be surrounded by a layer of amorphous polymer even at room temperature, and consequently the current model may be adequate at sufficiently high levels of confinement. Based on this premise, we qualitatively describe the variation of σ with ω reported in Zheng et al. [59]. In summary, we propose that the amorphous layer can be subdivided into two regions: bound and free amorphous polymer. While this is an oversimplification, it captures the fact that the closer a PEO chain is to the garnet the least flexible it is. This model qualitatively explains the relatively slow decay in ionic conductivity past the critical perco-

28

lation volume fraction ω_c, avoiding the power-law like decay obtained from the traditional core-shell EMT models that have been employed to explain conductivity enhancement in CSSEs with passive fillers. Yet, further quantitative work is required to validate this hypothesis.

While in any given system both garnet surfaces differ in the distribution of ions, key features such as the thickness of the Li^+-free layer (which largely coincides with the thickness of the rigidified polymer layer), differ by less than 1 nm between the opposing sides. Moreover, the shapes and thicknesses of the polymer shells bound to either surface are largely symmetric. Because these are the two most significant features impacting the Li^+ diffusivity under conditions of high confinement (at a constant LiTFSI concentration), we expect that the differences between the garnet surfaces do not alter the main conclusions from this study. Still, we recognize that local differences in the garnet surface must be impactful. A systematic examination of this effect should be investigated in future work.

Extensive simulations by Brooks et al.[30] have shown that $N = 100$ suffices to accurately predict the Li^+ diffusivity in bulk PEO(LiFTSI) for system with high molecular weight polymer. However, this may not be the case in the presence of inorganic inclusions. In that regard, our results constitute a qualitative exploration of the phenomena occurring in the vicinity of the filler surface. Examining large, $N \geq 100$ polymer chains should be explored in future works by using, for example, coarse-grained MD methods.

Upcoming studies will also focus on studying CSSEs below T_m, employing, for example, kinetic Monte Carlo methods to predict Li^+ diffusion through crystalline PEO.

9. Aknowledgements

References

[1] J. Janek, W. G. Zeier, A solid future for battery development, Nature Energy 1 (9) (2016) 16141. doi:10.1038/nenergy.2016.141.
URL https://doi.org/10.1038/nenergy.2016.141

[2] Q. Zhao, S. Stalin, C.-Z. Zhao, L. A. Archer, Designing solid-state electrolytes for safe, energy-dense batteries, Nature Reviews Materials 5 (3) (2020) 229–252. doi:10.1038/s41578-019-0165-5.
URL https://doi.org/10.1038/s41578-019-0165-5

[3] T. Placke, R. Kloepsch, S. Dühnen, M. Winter, Lithium ion, lithium metal, and alternative rechargeable battery technologies: the odyssey for high energy density, Journal of Solid State Electrochemistry 21 (7) (2017) 1939–1964. doi:10.1007/s10008-017-3610-7.
URL https://doi.org/10.1007/s10008-017-3610-7

[4] P. Albertus, V. Anandan, C. Ban, N. Balsara, I. Belharouak, J. Buettner-Garrett, Z. Chen, C. Daniel, M. Doeff, N. J. Dudney, B. Dunn, S. J. Harris, S. Herle, E. Herbert, S. Kalnaus, J. A. Libera, D. Lu, S. Martin, B. D. McCloskey, M. T. McDowell, Y. S. Meng, J. Nanda, J. Sakamoto, E. C. Self, S. Tepavcevic, E. Wachsman, C. Wang, A. S. Westover, J. Xiao, T. Yersak, Challenges for and pathways toward li-metal-based all-solid-state batteries, ACS Energy Letters 6 (4) (2021) 1399–1404. arXiv:https://doi.org/10.

1021/acsenergylett.1c00445, doi:10.1021/acsenergylett.1c00445.

₆₄₀   URL https://doi.org/10.1021/acsenergylett.1c00445

[5] S. Sen, E. Trevisanello, E. Niemller, B.-X. Shi, F. J. Simon, F. H. Richter, The role of polymers in lithium solid-state batteries with inorganic solid electrolytes, J. Mater. Chem. A 9 (2021) 18701–18732. doi:10.1039/D1TA02796D.

₆₄₅   URL http://dx.doi.org/10.1039/D1TA02796D

[6] T. Famprikis, P. Canepa, J. A. Dawson, M. S. Islam, C. Masquelier, Fundamentals of inorganic solid-state electrolytes for batteries, Nature Materials 18 (12) (2019) 1278–1291. doi:10.1038/s41563-019-0431-3.
URL https://doi.org/10.1038/s41563-019-0431-3

₆₅₀ [7] V. Thangadurai, S. Narayanan, D. Pinzaru, Garnet-type solid-state fast li ion conductors for li batteries: Critical review, Chemical Society Reviews 43 (2014) 4714–4727. doi:10.1039/C4CS00020J.

[8] M. R. Bonilla, F. A. García Daza, M. Fernández-Pendás, J. Carrasco, E. Akhmatskaya, Multiscale modelling and simulation of advanced battery ₆₅₅ materials, in: M. Cruz, C. Parés, P. Quintela (Eds.), Progress in Industrial Mathematics: Success Stories, Springer International Publishing, Cham, 2021, pp. 69–113.

[9] F. Aguesse, W. Manalastas, L. Buannic, J. M. Lopez del Amo, G. Singh, A. Llordés, J. Kilner, Investigating the dendritic growth during full cell ₆₆₀ cycling of garnet electrolyte in direct contact with li metal, ACS Applied Materials & Interfaces 9 (4) (2017) 3808–3816. arXiv:https://doi.org/10.1021/acsami.6b13925, doi:10.1021/acsami.6b13925.
URL https://doi.org/10.1021/acsami.6b13925

[10] K. Hofstetter, A. J. Samson, S. Narayanan, V. Thangadurai, Present ₆₆₅ understanding of the stability of li-stuffed garnets with moisture, carbon dioxide, and metallic lithium, Journal of Power Sources 390 (2018) 297 –

312. doi:https://doi.org/10.1016/j.jpowsour.2018.04.016.

URL http://www.sciencedirect.com/science/article/pii/S0378775318303598

[11] M. Vervaeke, G. Calabrese, Prospective design in the automotive sector and the trajectory of the bluecar project: An electric car sharing system, International Journal of Vehicle Design 68 (2015) 245. doi:10.1504/IJVD.2015.071083.

[12] T. Yang, J. Zheng, Q. Cheng, Y.-Y. Hu, C. K. Chan, Composite polymer electrolytes with li7la3zr2o12 garnet-type nanowires as ceramic fillers: Mechanism of conductivity enhancement and role of doping and morphology, ACS Applied Materials & Interfaces 9 (26) (2017) 21773–21780. arXiv:https://doi.org/10.1021/acsami.7b03806, doi:10.1021/acsami.7b03806.

URL https://doi.org/10.1021/acsami.7b03806

[13] H. Xu, P.-H. Chien, J. Shi, Y. Li, N. Wu, Y. Liu, Y.-Y. Hu, J. B. Goodenough, High-performance all-solid-state batteries enabled by salt bonding to perovskite in poly(ethylene oxide), Proceedings of the National Academy of Sciences 116 (38) (2019) 18815–18821. arXiv:https://www.pnas.org/content/116/38/18815.full.pdf, doi:10.1073/pnas.1907507116.

URL https://www.pnas.org/content/116/38/18815

[14] X. Yu, A. Manthiram, A review of composite polymer-ceramic electrolytes for lithium batteries, Energy Storage Materials 34 (2021) 282–300. doi:https://doi.org/10.1016/j.ensm.2020.10.006.

URL https://www.sciencedirect.com/science/article/pii/S2405829720303846

[15] F. Langer, I. Bardenhagen, J. Glenneberg, R. Kun, Microstructure and temperature dependent lithium ion transport of ceramic-polymer composite electrolyte for solid-state lithium ion batteries based on garnet-type li7la3zr2o12, Solid State Ionics 291 (2016) 8 – 13.

32

doi:https://doi.org/10.1016/j.ssi.2016.04.014.

URL http://www.sciencedirect.com/science/article/pii/S0167273816300625

[16] M. Keller, G. B. Appetecchi, G.-T. Kim, V. Sharova, M. Schneider, J. Schuhmacher, A. Roters, S. Passerini, Electrochemical performance of a solvent-free hybrid ceramic-polymer electrolyte based on li7la3zr2o12 in p(eo)15litfsi, Journal of Power Sources 353 (2017) 287 – 297. doi:https://doi.org/10.1016/j.jpowsour.2017.04.014.

URL http://www.sciencedirect.com/science/article/pii/S0378775317304913

[17] J. Zagórski, J. M. López del Amo, M. J. Cordill, F. Aguesse, L. Buannic, A. Llordés, Garnet-polymer composite electrolytes: New insights on local li-ion dynamics and electrodeposition stability with li metal anodes, ACS Applied Energy Materials 2 (3) (2019) 1734–1746. arXiv:https://doi.org/10.1021/acsaem.8b01850, doi:10.1021/acsaem.8b01850.

URL https://doi.org/10.1021/acsaem.8b01850

[18] J. Zheng, Y.-Y. Hu, New insights into the compositional dependence of li-ion transport in polymer-ceramic composite electrolytes, ACS Appl. Mater. Interfaces 10 (4) (2018) 4113–4120. doi:10.1021/acsami.7b17301.

[19] D. Brogioli, F. Langer, R. Kun, F. La Mantia, Space-charge effects at the li7la3zr2o12/poly(ethylene oxide) interface, ACS Applied Materials & Interfaces 11 (12) (2019) 11999–12007. arXiv:https://doi.org/10.1021/acsami.8b19237, doi:10.1021/acsami.8b19237.

URL https://doi.org/10.1021/acsami.8b19237

[20] A. Gupta, J. Sakamoto, Controlling ionic transport through the peo-litfsi/llzto interface 28 (2) (2019) 63–69. doi:10.1149/2.f06192if.

URL http://dx.doi.org/10.1149/2.F06192if

[21] J. Zhang, N. Zhao, M. Zhang, Y. Li, P. K. Chu, X. Guo, Z. Di, X. Wang, H. Li, Flexible and ion-conducting membrane electrolytes

725   for solid-state lithium batteries: Dispersion of garnet nanoparticles in insulating polyethylene oxide, Nano Energy 28 (2016) 447–454. doi:https://doi.org/10.1016/j.nanoen.2016.09.002.
URL https://www.sciencedirect.com/science/article/pii/S2211285516303640

730 [22] W. Liu, S. W. Lee, D. Lin, F. Shi, S. Wang, A. D. Sendek, Y. Cui, Enhancing ionic conductivity in composite polymer electrolytes with well-aligned ceramic nanowires, Nature Energy 2 (5) (2017) 17035. doi:10.1038/nenergy.2017.35.
URL https://doi.org/10.1038/nenergy.2017.35

735 [23] Z. Li, H.-M. Huang, J.-K. Zhu, J.-F. Wu, H. Yang, L. Wei, X. Guo, Ionic conduction in composite polymer electrolytes: Case of peo:gallzo composites, ACS Applied Materials & Interfaces 11 (1) (2019) 784–791. arXiv:https://doi.org/10.1021/acsami.8b17279, doi:10.1021/acsami.8b17279.
740   URL https://doi.org/10.1021/acsami.8b17279

[24] W. Wieczorek, M. Siekierski, A description of the temperature dependence of the conductivity for composite polymeric electrolytes by effective medium theory, Journal of Applied Physics 76 (4) (1994) 2220–2226. arXiv:https://doi.org/10.1063/1.357638, doi:10.1063/1.357638.
745   URL https://doi.org/10.1063/1.357638

[25] F. Croce, G. B. Appetecchi, L. Persi, B. Scrosati, Nanocomposite polymer electrolytes for lithium batteries, Nature 394 (6692) (1998) 456–458. doi:10.1038/28818.
URL https://doi.org/10.1038/28818

750 [26] A. Villa, J. C. Verduzco, J. A. Libera, E. E. Marinero, Ionic conductivity optimization of composite polymer electrolytes through filler particle chemical modification, Ionics 27 (6) (2021) 2483–2493. doi:10.1007/

s11581-021-04042-9.

URL https://doi.org/10.1007/s11581-021-04042-9

[27] S. Mogurampelly, V. Ganesan, Effect of nanoparticles on ion transport in polymer electrolytes, Macromolecules 48 (8) (2015) 2773–2786. arXiv: https://doi.org/10.1021/ma502578s, doi:10.1021/ma502578s.
URL https://doi.org/10.1021/ma502578s

[28] S. Mogurampelly, V. Ganesan, Influence of nanoparticle surface chemistry on ion transport in polymer nanocomposite electrolytes, Solid State Ionics 286 (2016) 57–65. doi:https://doi.org/10.1016/j.ssi.2015.12.018.
URL   https://www.sciencedirect.com/science/article/pii/S016727381530059X

[29] M. R. Bonilla, F. A. García Daza, P. Ranque, F. Aguesse, J. Carrasco, E. Akhmatskaya, Unveiling interfacial li-ion dynamics in li7la3zr2o12/peo(litfsi) composite polymer-ceramic solid electrolytes for all-solid-state lithium batteries, ACS Applied Materials & Interfaces 13 (26) (2021) 30653–30667. doi:10.1021/acsami.1c07029.
URL https://doi.org/10.1021/acsami.1c07029

[30] D. J. Brooks, B. V. Merinov, W. A. Goddard, B. Kozinsky, J. Mailoa, Atomistic description of ionic diffusion in peo-litfsi: Effect of temperature, molecular weight, and ionic concentration, Macromolecules 51 (21) (2018) 8987–8995. arXiv:https://doi.org/10.1021/acs.macromol.8b01753, doi:10.1021/acs.macromol.8b01753.
URL https://doi.org/10.1021/acs.macromol.8b01753

[31] R. Semino, N. A. Ramsahye, A. Ghoufi, G. Maurin, Microscopic model of the metal-organic framework/polymer interface: A first step toward understanding the compatibility in mixed matrix membranes, ACS Applied Materials & Interfaces 8 (1) (2016) 809–819, pMID: 26653765. arXiv:https://doi.org/10.1021/acsami.5b10150, doi:10.1021/acsami.5b10150.
URL https://doi.org/10.1021/acsami.5b10150

[32] M. Marzantowicz, J. Dygas, F. Krok, A. asiska, Z. Florjaczyk, E. Zygado-Monikowska, A. Affek, Crystallization and melting of peo:litfsi polymer electrolytes investigated simultaneously by impedance spectroscopy and polarizing microscopy, Electrochimica Acta 50 (19) (2005) 3969–3977, polymer Electrolytes. doi:https://doi.org/10.1016/j.electacta.2005.02.053.
URL https://www.sciencedirect.com/science/article/pii/S0013468605003270

[33] W. L. Jorgensen, D. S. Maxwell, J. Tirado-Rives, Development and testing of the opls all-atom force field on conformational energetics and properties of organic liquids, Journal of the American Chemical Society 118 (45) (1996) 11225–11236. arXiv:https://doi.org/10.1021/ja9621760, doi:10.1021/ja9621760.
URL https://doi.org/10.1021/ja9621760

[34] L. Meabe, S. R. Peña, M. Martinez-Ibañez, Y. Zhang, E. Lobato, H. Manzano, M. Armand, J. Carrasco, H. Zhang, Insight into the ionic transport of solid polymer electrolytes in polyether and polyester blends, The Journal of Physical Chemistry C 124 (33) (2020) 17981–17991. arXiv:https://doi.org/10.1021/acs.jpcc.0c04987, doi:10.1021/acs.jpcc.0c04987.
URL https://doi.org/10.1021/acs.jpcc.0c04987

[35] T. Köddermann, D. Paschek, R. Ludwig, Molecular dynamic simulations of ionic liquids: A reliable description of structure, thermodynamics and dynamics, ChemPhysChem 8 (17) (2007) 2464–2470. arXiv:https://chemistry-europe.onlinelibrary.wiley.com/doi/pdf/10.1002/cphc.200700552, doi:10.1002/cphc.200700552.
URL https://chemistry-europe.onlinelibrary.wiley.com/doi/abs/10.1002/cphc.200700552

[36] T.-C. Lim, Alignment of buckingham parameters to generalized lennard-jones potential functions, Zeitschrift für Naturforschung A 64 (3-4) (2009)

36

$200 - 204$. doi:https://doi.org/10.1515/zna-2009-3-406.
URL https://www.degruyter.com/view/journals/zna/64/3-4/article-p200.xml

[37] E. Akhmatskaya, S. Reich, Gshmc: An efficient method for molecular simulation, J. Comput. Phys. 227 (10) (2008) 4934 – 4954. doi:https://doi.org/10.1016/j.jcp.2008.01.023.
URL http://www.sciencedirect.com/science/article/pii/S0021999108000533

[38] A. Horowitz, A generalized guided monte carlo algorithm, Physics Letters B 268 (2) (1991) 247–252. doi:10.1016/0370-2693(91)90812-5.

[39] B. Escribano, E. Akhmatskaya, J. Mujika, Combining stochastic and deterministic approaches within high efficiency molecular simulations, Central European Journal of Mathematics 11 (4) (2013) 787–799. doi:10.2478/s11533-012-0164-x.

[40] M. Fernández-Pendás, E. Akhmatskaya, J. Sanz-Serna, Adaptive multistage integrators for optimal energy conservation in molecular simulations, Journal of Computational Physics 327 (2016) 434–449. doi:10.1016/j.jcp.2016.09.035.

[41] E. Akhmatskaya, M. Fernández-Pendás, T. Radivojević, J. M. Sanz-Serna, Adaptive splitting integrators for enhancing sampling efficiency of modified hamiltonian monte carlo methods in molecular simulation, Langmuir 33 (42) (2017) 11530–11542. doi:10.1021/acs.langmuir.7b01372.
URL https://doi.org/10.1021/acs.langmuir.7b01372

[42] S. Pronk, S. Páll, R. Schulz, P. Larsson, P. Bjelkmar, R. Apostolov, M. Shirts, J. Smith, P. Kasson, D. Van Der Spoel, B. Hess, E. Lindahl, Gromacs 4.5: A high-throughput and highly parallel open source molecular simulation toolkit, Bioinformatics 29 (7) (2013) 845–854. doi:10.1093/bioinformatics/btt055.

[43] F. A. García Daza, M. R. Bonilla, A. Llordés, J. Carrasco, E. Akhmatskaya, Atomistic insight into ion transport and conductivity in ga/al-substituted li$_7$la$_3$zr$_2$o$_{12}$ solid electrolytes, ACS Applied Materials & Interfaces 11 (1) (2019) 753–765. `doi:10.1021/acsami.8b17217`.

[44] M. R. Bonilla, F. A. García Daza, J. Carrasco, E. Akhmatskaya, Exploring li-ion conductivity in cubic, tetragonal and mixed-mhase al-substituted li$_7$la$_3$zr$_2$o$_{12}$ using atomistic simulations and effective medium theory, Acta Mater. 175 (2019) 426 – 435. `doi:https://doi.org/10.1016/j.actamat.2019.06.033`.

[45] L. Martínez, R. Andrade, E. G. Birgin, J. M. Martínez, Packmol: A package for building initial configurations for molecular dynamics simulations, J. Comput. Phys. 30 (13) (2009) 2157–2164. `doi:10.1002/jcc.21224`.
URL `https://onlinelibrary.wiley.com/doi/abs/10.1002/jcc.21224`

[46] B. Hess, P-lincs: A parallel linear constraint solver for molecular simulation, J. Chem. Theory Comput. 4 (1) (2008) 116–122. `doi:10.1021/ct700200b`.
URL `https://doi.org/10.1021/ct700200b`

[47] J. Kästner, Umbrella sampling, WIREs Computational Molecular Science 1 (6) (2011) 932–942. `arXiv:https://wires.onlinelibrary.wiley.com/doi/pdf/10.1002/wcms.66`, `doi:https://doi.org/10.1002/wcms.66`.
URL `https://wires.onlinelibrary.wiley.com/doi/abs/10.1002/wcms.66`

[48] S. Kumar, J. M. Rosenberg, D. Bouzida, R. H. Swendsen, P. A. Kollman, The weighted histogram analysis method for free-energy calculations on biomolecules. i. the method, Journal of Computational Chemistry 13 (8) (1992) 1011–1021. `arXiv:https://onlinelibrary.wiley.com/doi/pdf/10.1002/jcc.540130812`, `doi:https://doi.org/10.1002/jcc.540130812`.
URL `https://onlinelibrary.wiley.com/doi/abs/10.1002/jcc.540130812`

[49] R. C. Dutta, S. K. Bhatia, Structure and gas transport at the polymer-zeolite interface: Insights from molecular dynamics simulations, ACS Applied Materials & Interfaces 10 (6) (2018) 5992–6005, pMID: 29350032. `arXiv:https://doi.org/10.1021/acsami.7b17470`, `doi:10.1021/acsami.7b17470`.
URL `https://doi.org/10.1021/acsami.7b17470`

[50] Y. Li, Y. Zhao, Y. Cui, Z. Zou, D. Wang, S. Shi, Screening polyethylene oxide-based composite polymer electrolytes via combining effective medium theory and halpin-tsai model, Computational Materials Science 144 (2018) 338 – 344. `doi:https://doi.org/10.1016/j.commatsci.2017.12.014`.
URL `http://www.sciencedirect.com/science/article/pii/S0927025617306997`

[51] A. Maitra, A. Heuer, Cation transport in polymer electrolytes: A microscopic approach, Phys. Rev. Lett. 98 (2007) 227802. `doi:10.1103/PhysRevLett.98.227802`.
URL `https://link.aps.org/doi/10.1103/PhysRevLett.98.227802`

[52] S. Mogurampelly, O. Borodin, V. Ganesan, Computer simulations of ion transport in polymer electrolyte membranes, Annual Review of Chemical and Biomolecular Engineering 7 (1) (2016) 349–371, pMID: 27070764. `arXiv:https://doi.org/10.1146/annurev-chembioeng-080615-034655`, `doi:10.1146/annurev-chembioeng-080615-034655`.
URL `https://doi.org/10.1146/annurev-chembioeng-080615-034655`

[53] D. Roilo, P. N. Patil, R. S. Brusa, A. Miotello, S. Aghion, R. Ferragut, R. Checchetto, Polymer rigidification in graphene based nanocomposites: Gas barrier effects and free volume reduction, Polymer 121 (2017) 17–25. `doi:https://doi.org/10.1016/j.polymer.2017.06.010`.
URL `https://www.sciencedirect.com/science/article/pii/S0032386117305700`

[54] S. G. Falkovich, V. M. Nazarychev, S. V. Larin, J. M. Kenny, S. V. Lyulin, Mechanical properties of a polymer at the interface structurally ordered by graphene, The Journal of Physical Chemistry C 120 (12) (2016) 6771–6777. `arXiv:https://doi.org/10.1021/acs.jpcc.5b11028`, `doi: 10.1021/acs.jpcc.5b11028`.
URL `https://doi.org/10.1021/acs.jpcc.5b11028`

[55] P. Liu, E. Harder, B. J. Berne, On the calculation of diffusion coefficients in confined fluids and interfaces with an application to the liquid-vapor interface of water, The Journal of Physical Chemistry B 108 (21) (2004) 6595–6602. `doi:10.1021/jp0375057`.

[56] K. Timachova, H. Watanabe, N. P. Balsara, Effect of molecular weight and salt concentration on ion transport and the transference number in polymer electrolytes, Macromolecules 48 (21) (2015) 7882–7888. `arXiv: https://doi.org/10.1021/acs.macromol.5b01724`, `doi:10.1021/acs. macromol.5b01724`.
URL `https://doi.org/10.1021/acs.macromol.5b01724`

[57] H. Lee, A. H. de Vries, S.-J. Marrink, R. W. Pastor, A coarse-grained model for polyethylene oxide and polyethylene glycol: Conformation and hydro-dynamics, The Journal of Physical Chemistry B 113 (40) (2009) 13186–13194, pMID: 19754083. `arXiv:https://doi.org/10.1021/jp9058966`, `doi:10.1021/jp9058966`.
URL `https://doi.org/10.1021/jp9058966`

[58] B. Hanson, V. Pryamitsyn, V. Ganesan, Mechanisms underlying ionic mobilities in nanocomposite polymer electrolytes, ACS Macro Letters 2 (11) (2013) 1001–1005. `arXiv:https://doi.org/10.1021/mz400234m`, `doi:10.1021/mz400234m`.
URL `https://doi.org/10.1021/mz400234m`

[59] J. Zheng, M. Tang, Y.-Y. Hu, Lithium ion pathway within li7la3zr2o12-polyethylene oxide composite electrolytes, Angewandte Chemie In-

40

ternational Edition 55 (40) (2016) 12538–12542.   `arXiv:https://onlinelibrary.wiley.com/doi/pdf/10.1002/anie.201607539`, `doi:10.1002/anie.201607539`.

URL `https://onlinelibrary.wiley.com/doi/abs/10.1002/anie.201607539`

[60] F. Croce, G. B. Appetecchi, L. Persi, B. Scrosati, Nanocomposite polymer electrolytes for lithium batteries, Nature 394 (6692) (1998) 456–458. `doi:10.1038/28818`.

URL `https://doi.org/10.1038/28818`

[61] W. Wieczorek, K. Such, H. Wyciślik, J. Plocharski, Modifications of crystalline structure of peo polymer electrolytes with ceramic additives, Solid State Ionics 36 (3) (1989) 255–257. `doi:https://doi.org/10.1016/0167-2738(89)90185-9`.

URL `https://www.sciencedirect.com/science/article/pii/0167273889901859`

[62] C.-W. Nan, D. M. Smith, A.c. electrical properties of composite solid electrolytes, Materials Science and Engineering: B 10 (2) (1991) 99–106. `doi:https://doi.org/10.1016/0921-5107(91)90115-C`.

URL `https://www.sciencedirect.com/science/article/pii/092151079190115C`